



23 km long and contain lava tubes that have rugged basal contacts defined by $\sim 90 \pm 23$ m high erosional
24 ramps. We suggest the lava flows eroded down into and were emplaced at shallow sub-surface
25 depths within wet, unconsolidated, near-seafloor sediments. Extrusion dynamics were likely
26 controlled by low magma viscosities, high hydrostatic pressures, and soft, near-seabed sediments,
27 which collectively are characteristic of deep-water environments. Because the lava flows and
28 volcanic edifices are imaged in 3D, we calculate the lava flows account for 50–97% of the total
29 erupted volume. Our results indicate deep-water volcanic edifices may thus form a minor
30 component (~ 3 –50%) of the extrusive system, and that accurate estimates of erupted volume
31 requires knowledge of the basal surface of genetically related lava flows. We conclude that 3D
32 seismic reflection data is a powerful tool for constraining the geometry and extrusion dynamics of
33 buried, deep-water volcanic features; such data should be used to image and quantify extrusion
34 dynamics of modern deep-water volcanoes.

35

36 **Keywords**

37 Volcano, deep-water, lava flow, seismic reflection, South China Sea

38

39 **1. Introduction**

40 The external morphology of volcanoes and their eruptive products reflect, and provide insights
41 into, the processes controlling magma extrusion and volcano construction (e.g. Walker, 1993;
42 Planke et al., 2000; Grosse and Kervyn, 2018). By extracting high-resolution, quantitative data on
43 the morphology of modern and, in some cases, still active volcanic edifices and surrounding lava
44 flows from airborne/shuttle radar topography or time-lapse multi-beam bathymetry, we can estimate



45 erupted volume and reconstruct volcano growth mechanisms (e.g. Holcomb et al., 1988; Walker,
46 1993; Goto and McPhie, 2004; Cocchi et al., 2016; Somoza et al., 2017; Allen et al., 2018; Grosse
47 and Kervyn, 2018). Whilst remote sensing data capture the external morphology of volcanoes and
48 lava flows, they do not image their basal surface or internal architecture. Without access to the full
49 3D structure of these extrusive systems, it is difficult to assess the accuracy of estimated volumes
50 of erupted material, or test volcano growth and lava emplacement models.

51 Several studies demonstrate that seismic reflection data can be used to map the external
52 morphology and internal architecture of buried volcanoes in 3D (e.g. Planke et al., 2000; Calvès et
53 al., 2011; Jackson, 2012; Magee et al., 2013; Reynolds et al., 2017). To-date, most seismic-based
54 studies have focused on volcanoes formed in sub-aerial or shallow-marine environments (e.g.
55 Planke et al., 2000; Jackson, 2012; Magee et al., 2013; Reynolds et al., 2018), although seismic
56 reflection surveys have been used to image the shallowly buried flanks of deep-water volcanoes (e.g.
57 Funck et al. 1996). The 3D geometry, internal structure, extrusion dynamics, and volume of deep-
58 water volcanoes thus remain poorly documented.

59 We use high-resolution 3D seismic reflection data to examine the external morphology and
60 internal architecture of two, Late Miocene-Quaternary submarine volcanoes that were emplaced in
61 deep-water (>2.0 km) on highly stretched continental crust in the northern South China Sea (Fig. 1).
62 The volcanoes and associated lava flows are now buried by a ~55–330 m thick sedimentary
63 succession (Fig. 1). By interpreting volcano and lava flow 3D structure, distribution, and size, we
64 aim to determine extrusion dynamics, calculate accurate erupted volumes, and relate our findings to
65 deep-water volcanoes studied using bathymetry and remote sensing data. We show basal surfaces
66 of volcanic edifices and lava flows are rugged, with 50–97% of the total erupted material hosted



67 within the latter; i.e. the volcano edifices only comprise only a small portion of the total erupted
68 magma volume. We suggest the high hydrostatic pressure of the deep-water environment controlled
69 erupting lava rheology and, consequently, volcano and lava flow morphology and run-out distance.
70 Our results also show erupted volumes calculated from airborne/shuttle radar topography or time-
71 lapse multi-beam bathymetry data, which typically assume imaged volcanoes and lava flows have
72 a smooth base, may be grossly underestimated.

73

74 **2. Geological setting**

75 The study area is located in the south of Pearl River Mouth Basin, on the northern, highly
76 stretched continental crust of the South China Sea (Franke, 2013; Zhao et al., 2016) (Fig. 1a). The
77 South China Sea was an area of subduction in the late Mesozoic, before the onset of continental
78 rifting and subsequent seafloor spreading (~33-15 Myr) in the Cenozoic (e.g. Taylor and Hayes,
79 1983; Briaies et al., 1993; Franke et al., 2014; Li et al., 2014; Sun et al., 2014a; Ding and Li, 2016).
80 A lack of seaward-dipping reflections (SDRs), and low volumes of rift-related igneous rocks,
81 suggest the northern part of the South China Sea is a magma-poor margin (e.g. Clift et al., 2001;
82 Yan et al., 2006; Cameselle et al., 2017). Seafloor spreading ceased at ~15 Ma (Li et al., 2014), with
83 post-rift thermal cooling driving subsidence of the northern South China Sea margin since the Early
84 Miocene (Ru and Pigott, 1986; Yu, 1994). During this phase of thermal subsidence the Dongsha
85 Event (~5.3 Ma) occurred, which involved widespread uplift and normal faulting (e.g. Lüdmann et
86 al., 2001). Several mechanisms may have triggered the Dongsha Event, including the collision
87 between Taiwan and the East Asian continent (Lüdmann et al., 2001; Hall, 2002), isostatic rebound
88 (Zhao et al., 2012), post-rift magmatism (Franke, 2013), lithospheric bending (Wu et al., 2014),



89 and/or subduction of the South China Sea beneath the Philippine Sea plate (Xie et al., 2017).

90 Post-spreading magmatism in the South China Sea may reflect ascent of magma triggered by

91 subduction of the South China Sea along the Manila trench and collision with Taiwan Island

92 (Lüdmann et al., 2001), convective removal of continental lithosphere by warm asthenosphere

93 (Lester et al., 2014), or magma ascent from a high-velocity layer in the lower crust fed by the Hainan

94 mantle plume (Xia et al., 2016; Fan et al., 2017). Volcanoes generated by post-rift magmatism in

95 the early Miocene and Quaternary were emplaced both onshore and offshore (e.g. Zou et al., 1995;

96 Yan et al., 2006; Franke, 2013; Li et al., 2014; Sun et al., 2014b; Zhao et al., 2014, 2016; Fan et al.,

97 2017), with the latter typically extruded onto the continental slope in relatively shallow water depths

98 (<300 m; Yan et al., 2006; Zhao et al., 2016). Boreholes reveal these shallow-water volcanoes are

99 composed of basalt, dacite, and rhyolitic tuff (Li and Liang, 1994; Yan et al., 2006; Zhao et al.,

100 2016). In addition to the onshore and shallow-water volcanoes, several volcanoes were emplaced

101 further basinwards on the continental slope in deeper water, close to the Continent-Ocean Boundary

102 (COB) (Clift et al., 2001; Wang et al., 2006; Cameselle et al., 2017) (Fig. 1). We examine two of

103 these deep-water volcanoes, which are situated in an area currently characterized by water depths

104 of 1850–2680 m and that are now buried by sedimentary strata up to 330 m thick (Fig. 1).

105 Micropalaeontological data from the Pearl River Mouth Basin (Xu et al., 1995; Qin, 1996), and

106 microfauna data from ODP sites 1146 and 1148, indicate the Middle Miocene (16.5 Ma) to Recent,

107 nanofossil-bearing clays encasing the volcanoes were deposited in a deep-water setting (1.0–3.0 km;

108 Wang et al., 2000).

109

110 **3. Data and Methods**



111 We use a time-migrated 3D seismic reflection survey acquired in 2012 and covering an area of
112 $\sim 350 \text{ km}^2$ (Fig. 1b). The seismic data are zero-phase processed and displayed with SEG (Society of
113 Exploration Geophysicists) normal polarity, whereby a downward increase in acoustic impedance
114 (a function of rock velocity and density) corresponds to a positive reflection event (red on seismic
115 profiles) (e.g. Brown, 2004). Bin spacing is 25 m, and the seismic data have a dominant frequency
116 in the interval of interest (i.e. 0–400 ms two-way time (tw)) of $\sim 40 \text{ Hz}$.

117 Stacking velocities are not available for the survey and no wells intersect the studied Late
118 Miocene-Quaternary, buried, deep-water volcanic features. We thus have no direct control on the
119 composition or velocities of the seismically imaged volcanic materials. Depth-conversion of
120 volcano and lava flow thickness measurements in milliseconds (tw) to meters is therefore based on
121 velocity estimates, which introduces some uncertainty into our erupted volume calculations. To
122 derive a reasonable velocity estimate, we use velocity data for submarine volcanoes obtained from
123 boreholes (i.e. BY7-1 and U1431) (Li et al., 2015; Zhao et al., 2016) and OBS (Ocean Bottom
124 Seismometer) profiles (Yan et al., 2001; Wang et al., 2006; Chiu, 2010; Wei et al., 2011) in the
125 South China Sea. The boreholes, which are situated $>300 \text{ km}$ away from our study area, intersect
126 buried basaltic volcanoes with p-wave velocities of $\sim 4.5 \text{ km/s}$ (BY7-1; Zhao et al., 2016) and ~ 3.0 –
127 5.0 km/s (IODP U1431; Li et al., 2015). OBS profiles reveal submarine volcanoes located 140 km
128 from the study area (Fig. 1a) typically have p-wave velocities of $>3.0 \text{ km/s}$, and occasionally up to
129 $\sim 5.5 \text{ km/s}$ (Yan et al., 2001; Wang et al., 2006; Chiu, 2010; Wei et al., 2011). The basaltic
130 composition and p-wave velocities of ~ 3.0 – 5.5 km/s for volcanoes intersected by boreholes and
131 studied using OBS data are consistent with p-wave velocity data for shallow-water, mafic volcanoes
132 located offshore western India (~ 3.3 – 5.5 km/s ; Calvès et al., 2011), and southern Australia in the



133 Bight (~2.4–6.7 km/s, with an average velocity of 4.0 km/s; Magee et al. 2013) and Bass (~2.2–4.0
134 km/s with an average of 3.0 km/s; Reynolds et al. 2018) basins. Based on these velocity data, we
135 assume the imaged volcanic material studied here have mafic compositions and p-wave velocities
136 of 4.0 (± 1.0) km/s. It is important to note that using a range of estimated velocities does not affect
137 our calculation of the *relative* amount of material contained within volcanic edifices versus the
138 flanking lava flows.

139 We calculate a vertical resolution ($\lambda/4$) of ~10 m for the sedimentary strata encasing the volcanic
140 materials, given a dominant frequency of 40 Hz and assuming a seismic velocity of 2.2 km/s for the
141 nanofossil-bearing clay (based on seismic refraction profiles OBS1993, Yan et al., 2001; OBS2001,
142 Wang et al., 2006; OBS2006-3, Wei et al., 2011). The calculated vertical resolution for the volcanic
143 materials is 19–31 m, based on a dominant frequency of 40 Hz and estimated seismic velocities of
144 4.0 (± 1.0) km/s. The top and base of volcanic structures can be distinguished in seismic reflection
145 data when their thickness is greater than the estimated vertical resolution of these data (i.e. 19–31
146 m) (Brown, 2004). Volcanic structures with thicknesses below the vertical resolution, but above the
147 detection limit (i.e. $\lambda/8 = 10\text{--}16$ m), are imaged as tuned reflection packages whereby reflections
148 from their top and base contacts interfere on their return to the surface and cannot be distinguished
149 (Brown, 2004). The lava flows are typically >2 seismic reflection thick ($>41\pm 10$ m), suggesting
150 they too are thicker than the tuning thickness and are represented by discrete top and basal
151 reflections (Tables 1-3).

152 We used a regional 2D seismic profile and interpreted four seismic surfaces tied to ODP Site 1146,
153 which is located ~65 km west of the study area (Figs. 1a, 2), and two horizons locally mappable
154 around the volcanoes: T0 (~2.58 Ma), T1 (~5.3 Ma), TRa (~6.5 Ma), and TRb (~8.2 Ma), TM (top



155 of the volcanic material) and BM (base of the volcanic material). The youngest age of the volcanoes
156 and associated lava flows are determined using the first seismic reflection that onlaps or overlies
157 them (Fig. 3). After mapping TM and BM, we calculated the volumes of the volcanic features
158 (Tables 1-4), with errors largely arising from uncertainties in the velocities (4.0 ± 1.0 km/s) used to
159 undertake the depth conversion (see above).

160 Root mean square (RMS) amplitude extractions and slices through a variance volume were used
161 to constrain the geometry, scale, and distribution of the submarine volcanoes (Figs. 3-8). The RMS
162 amplitude attribute computes the square root of the sum of squared amplitudes, divided by the
163 number of samples within the specified window used; put simply, the RMS attribute measures the
164 reflectivity of a given thickness of seismic data (Fig. 4a) (Brown, 2004). The variance attribute is
165 free of interpreter bias because it is directly derived from the processed data (Fig. 5). Variance
166 measures the variability in shape between seismic traces; this can be done in a specified window
167 along a picked horizon or within a full 3D seismic volume. Variance is typically used to map
168 structural and stratigraphic discontinuities related to, for example, faults and channels (Brown,
169 2004).

170

171 **4. Seismic expression and interpretation of igneous features**

172

173 **4.1. Observations**

174 We identify three main types of seismic structures and associated facies: (1) Seismic Facies 1
175 (SF1) - two (V1 and V2) conical-shaped features up to ~ 202 ms twt ($\sim 404 \pm 101$ m) thick, which
176 internally are weakly-to-moderately reflective or chaotic with distinguished reflections



177 downlapping onto BM, capped by a positive polarity, high-amplitude reflection (TM) overlapped by
178 overlying strata (Figs. 3a, 7); (2) Seismic Facies 2 (SF2) - ribbon-like, broadly strata-concordant,
179 high-amplitude, positive polarity reflections, which emanate from the conical structures (SF1) and
180 extend up to ~9.2 km downslope (Figs. 3a-b, 6-7); and (3) Seismic Facies 3 (SF3) - saucer-shaped,
181 strata-discordant, high-amplitude reflections situated beneath SF1 and SF2 (Fig. 6).

182

183 **4.2. Interpretations**

184 The conical shape of SF1 and downlap of its internal reflections (where developed) onto BM,
185 coupled with onlap of overlying reflections onto TM, suggest SF1 is an extrusive rather than
186 intrusive feature. SF1 is similar in terms of its conical shape, highly reflective top, and internally
187 chaotic reflections to mud volcanoes documented elsewhere in the northern South China Sea (Sun
188 et al., 2012; Yan et al., 2017). It is therefore plausible SF1 could represent a mud volcano that fed
189 long run-out mud flows (i.e. SF2). Alternatively, the highly reflective, ribbon-like geometry of SF2
190 is similar to that associated with shallow/free gas accumulations (Sun et al., 2012). We consider
191 these two interpretations unlikely because: (i) the limited supply and high viscosity of mud means
192 mud volcanoes are rarely associated with long run-out flows, although we note that one mud flow
193 in the Indus Fan was ~5.0 km long (Calvès et al. 2009); and (ii) the top of SF2 is defined by a
194 positive polarity reflection (downward increase in acoustic impedance), which is opposite to that
195 typically associated with shallow/free gas accumulations (e.g. Judd and Hovland, 2007; Sun et al.,
196 2012). Based on their geometric and geophysical characteristics, spatial relationships, and similarity
197 to structures observed on other rifted continental margins, we interpret these features as volcanic
198 edifices (SF1), genetically related lava flows (SF2), and saucer-shaped sills (SF3) (e.g. Berndt et al.,



199 2000; Planke et al., 2000; Thomson and Hutton, 2004; Calvès et al., 2011; Jackson, 2012; Magee et
200 al., 2013; Reynolds et al., 2018). We now focus on the detailed external morphology and internal
201 architecture of the two deep-water volcanoes that are shallowly buried (<330 m) and thus well-
202 imaged.

203

204 **4.3. Volcano edifice 1 (V1) and associated lava flows**

205 V1 is a prominent, ~202 ms twt high (404 ± 101 m) and ~3.0 km diameter conical volcano covering
206 ~7.2 km², with a volume of $\sim 0.94 \pm 0.24$ km³ and an average flank dip of $\sim 15.0 \pm 3.6^\circ$ (Figs. 3-4;
207 Table 1). V1 is overlapped by overlying reflections, with the oldest onlapping reflection correlating
208 to TRa (~6.5 Ma); this suggests V1 was emplaced in the latest Miocene-earliest Pliocene (Fig. 3a).
209 V1 is underlain by a downward-tapering, >1.1 km deep, up to 2.0 km wide, sub-vertical zone of
210 chaotic reflections (Fig. 3a). We attribute the poor imaging within this chaotic sub-vertical zone to:
211 (1) the presence of sub-vertical feeder intrusions that disrupt background reflections and scatter
212 energy (cf. Thomson, 2007); (2) increased fluid flow and hydrothermal alteration in fractured and
213 deformed host rock adjacent to the magma plumbing system; and/or (3) scattering of energy
214 travelling through the volcano, leading to ‘wash-out’ of the underlying data (i.e. a geophysical
215 artefact; Magee et al. 2013). This reduction in imaging beneath the volcanoes partly obscures their
216 basal surface, but where visible it is clear BM undulates and truncates underlying stratal reflections
217 (Fig. 3b).

218 Volcano V1 is surrounded by an asymmetric apron of moderate-to-high amplitude reflections
219 extending up to 1.5 km from the main edifice. The apron is up to ~115 ms twt thick ($\sim 230 \pm 58$ m),
220 and has a dip of $< 0.5^\circ$ (Figs. 4a-b; Table 2). A package of moderate-to-very high-amplitude



221 reflections extending a further c. 1.5 km down-dip of this apron contains very high-amplitude,
222 channel-like geometries (marked with C1-C3 in (Fig. 4a), which terminate down-dip into or are
223 flanked at prominent bends by, moderate-amplitude, fan-like geometries (marked with F1-F4 in Fig.
224 4a). We interpret these two features as lava flow channels and fans, respectively (Fig. 3-4). The lava
225 flow channels are sinuous, <340 m wide, and usually bisect the lava fans (Figs 4a-b). Lava flow-
226 related features (i.e. apron, channels, and fans) emanating from V1 cover an area of ~14 km² (Tables
227 3-4), have an average thickness of ~33 ms twt (~66±17 m), and a volume of ~0.92±0.23 km³; this
228 volume is nearly equal to that of V1 (~0.94±0.24 km³) and thus represents ~50% of the total erupted
229 volume (~1.86±0.47 km³).

230

231 **4. 4. Volcano edifice 2 (V2) and associated lava flows**

232 V2 covers ~0.44 km² and is elliptical in plan-view, with long and short axes of ~1.2 km and ~0.6
233 km, respectively (Figs. 5, 7). The volcano is ~100 ms twt high (~200±50 m), with an irregular base,
234 has flank dips of ~27.8±5.9°, and a volume of 0.03±0.01 km³ (Figs. 5, 7; Table 1). The top of V2 is
235 of moderate amplitude and is irregular, with the oldest onlapping reflections correlating to Reflector
236 T1 (~5.3 Ma) suggesting V2 is latest Miocene-earliest Pliocene, but probably younger than V1 (Fig.
237 7). Reflections within V2 are chaotic and, similar to V1, V2 is underlain by a vertical zone of
238 disturbance (Fig. 7). V2 lacks a lava apron, instead being directly flanked by relatively straight, up
239 to 9.2 km long lava flow channels on its south-eastern side (C4-C7) (Fig. 5a). Lava flow C6 is
240 unusual in that underlying strata are truncated at the base of the flow, defining ‘ramps’ that are up
241 to ~32.5 ms twt high (~65±16 m) high and dip towards V2 at ~25.5±5.8° (Fig. 8). Beyond the main
242 ramp at the base of lava flow C6 (Fig. 5b), the lava flows thicken to ~130 ms twt (~260±65 m),



243 where it is defined by stacked, high-amplitude reflections that have a lobate geometry in plan-view
244 (F5) (Figs. 5, 7, 8c-d). At its distal end, the pinch out of F5 occurs where it abuts a basal ramp that
245 is $\sim 90 \pm 23$ m tall and that dips $\sim 9.3 \pm 2.3^\circ$ (Figs. 8c-d). F5 is capped by a younger lava fan (F6) (Figs.
246 8c-d). The V2-sourced lava flows (C4-C7 and F5) cover ~ 11.5 km²; ~ 4.20 km² of this comprises
247 lava flow channels and ~ 7.32 km² lava fan. Given the average thickness of the lava flow channels
248 ($\sim 61 \pm 16$ m) and fans ($\sim 109 \pm 27$ m), we estimate the total volume of V2-sourced lava flows to be
249 $\sim 1.05 \pm 0.27$ km³; this volume estimate is ~ 35 times greater than that of the main V2 edifice
250 (0.03 ± 0.01 km³), representing $\sim 97\%$ of the total erupted volume.

251

252 **4.5. Shallow sills and associated lava flows**

253 South of V2, we map two areally extensive, partly merged lava flows emanating from the upper
254 tips of inclined sheets fringing saucer-shaped sills (i.e. S1 and S2) (Figs. 1b, 5-6). A narrow, vertical,
255 seismically chaotic/blanking zone occurs directly below the saucer-shaped sills (Fig. 6). Several
256 linear structures, rooted at the junction between sills, and feeding the overlying lava fan (F6), are
257 also observed (Fig. 6). F6 covers an area of ~ 49 km², with a diameter of ~ 7.9 km and thickness of
258 55 ± 14 m (Table 4). F6 is directly overlapped by surface T0 (~ 2.58 Ma), suggesting it was emplaced
259 in the latest Pliocene (Fig. 6). Similar to other lava fans, F6 is characterized by a single, positive,
260 high-amplitude seismic event (Fig. 6). F6 extends beyond the seismic coverage and is much bigger
261 than other lava fans imaged in the study area (Figs. 5-6; Table 4).

262

263 **5. Discussion**

264 **5.1. Water depths during volcano emplacement**



265 The different burial depths and onlap relationships of the volcano edifices and lava flows studied
266 here suggest three phases of volcanism: i.e. ~6.5 Ma for V1, ~5.3 Ma for V2, and ~2.58 Ma for
267 S1/S2 (Figs. 2-3, 6-7). According to the relative sea-level change curve of the Pearl River Mouth
268 Basin acquired from nannofossils (Xu et al., 1995; Qin, 1996) and the dating of volcanic phases, the
269 water depths during V1 and V2 emplacement were likely ~75 m and ~150 m shallower than the
270 present depths of ~2.25 km and ~2.14 km, respectively. The water depth during the emplacement of
271 F6, fed by S1/S2, was probably ~150 m greater than the present depth of ~2.32 km (Xu et al., 1995;
272 Qin, 1996). To be conservative, we estimate that volcanism in the study area occurred in water
273 depths of a little over 2.0 km.

274

275 **5.2. Origin of post-spreading volcanism in the SCS**

276 The volcanoes documented here (~6.3–2.58 Ma) have similar ages with those documented in the
277 Hainan Island (e.g. Tu et al., 1991; Shi et al., 2011) and southwestern SCS (e.g. Li et al., 2013) (Fig.
278 1a). However, our volcanoes are substantially younger than those previously observed in the central
279 SCS (~13.8–7.0 Ma; Expedition 349 Scientists, 2014; Li et al., 2015) and on the middle-lower slope
280 of the northern SCS (~23.8–17.0 Ma; Yan et al., 2006; Zhao et al., 2016; Fan et al., 2017). We note
281 such small-scale, buried, post-spreading volcanic features studied here have not been identified by
282 lower-resolution techniques (e.g. gravity, magnetism, OBS and 2D seismic data). These young
283 volcanic features maybe widespread and diagnostic of post-spreading magmatism across the
284 northern SCS (e.g. Briais et al., 1993; Yan et al., 2006).

285 Given that the volcanoes documented here were emplaced after SCS rifting (>32 Ma ago; e.g.
286 Taylor and Hayes, 1983; Franke et al., 2014; Li et al., 2015) and spreading (>15 Ma ago; Li et al.,



287 2014), it is clear they have a different origin to the breakup-related volcanoes described elsewhere
288 (e.g. Yan et al., 2006; Expedition 349 Scientists, 2014; Li et al., 2015; Zhao et al., 2016; Fan et al.,
289 2017). The post-spreading age of volcanism may suggest that mantle melting (Clift et al., 2001) and
290 convective removal of continental lithosphere by warm asthenosphere (Lester et al., 2014),
291 processes typically associated with rifting and breakup, were not responsible for the generation of
292 this phase of igneous activity. Magmatism gets younger south-eastwards, from ~23.8–17.0 Ma on
293 the proximal continental slope (Yan et al., 2006; Zhao et al., 2016; Fan et al., 2017) to ~6.30–2.58
294 Ma in the deeper water study area. This observation is seemingly in agreement with the results of
295 teleseismic imaging, which shows southeastward migration of the eastern branch of the Hainan
296 mantle plume (Xia et al., 2016). This suggests that plume melt (Xia et al., 2016; Fan et al., 2017)
297 may have supplied magma to the observed volcanoes. However, where the Hainan mantle plume
298 was located or even whether the Hainan mantle plume occurred or not are still questioned at present
299 (e.g. Wheeler and White, 2000; He and Wen, 2011; Zhang and Li, 2018). Another possibility for
300 the origin of magma is related to the Dongsha Event that likely triggered the upwelling of mantle
301 materials as well as transtensional faulting (Lüdmann et al., 1999). The Dongsha Event peaked at
302 ~5.3 Ma and 2.58 Ma (Lüdmann et al., 2001) and was broadly synchronous with the main period of
303 eruptive magmatism documented here. Faults generated during the Dongsha Event may have
304 provided high-permeability zones that promoted the vertical migration of magma that fed the
305 eruptive centers.

306

307 **5.3. Volcano construction**

308 Both V1 and V2 are underlain by sub-vertical, pipe-like zones of chaotic reflections, which we



309 suggest demarcate the limits of their magma plumbing systems. The basal surfaces of V1 and V2
310 truncate underlying strata (Figs. 3a, 7). Apparent erosion of the sub-volcanic substrate may indicate
311 the initial eruptions were explosive, similar to eye-shaped hydrothermal vents documented by, for
312 example, Hansen et al. 2006; Magee et al. 2016). Alternatively, subsidence of the volcano load into
313 underlying, wet, unconsolidated sediments may have caused the strata to locally compact and
314 thereby change the reflection configuration, making it appear that they are truncated.

315 Internal reflections that lie sub-parallel to the flanks of V1 and V2 suggest the volcanoes grew by
316 increasing both edifice height and diameter by the accretion of volcanic material (Magee et al. 2013).
317 Flank dips of $\sim 15\text{--}28^\circ$ likely indicate that the volcanic material building the edifices constitutes
318 coherent lava flows and/or a dome structure, rather than a pyroclastic cone of tephra (Francis and
319 Thorpe, 1974; Griffiths and Fink, 1992). Construction via emplacement of coherent lava flows is
320 consistent with the presence of internal reflections in V1 and V2; i.e. boundaries between blocky
321 lava flows would be irregular and scatter seismic energy, meaning they would not likely be imaged.
322

323 **5.4. Lava flow extrusion dynamics**

324 In addition to the formation of volcanic edifices, both V1 and V2, as well as S1 and S2, are
325 associated with extensive lava flows. In particular, we show V1 and V2 are flanked either by an
326 asymmetric lava apron, which is broader on their downslope (SE) side, or lava flow channels that
327 flowed south-eastwards for up to >9 km (Figs. 3a, 4a-b, 5a). At sub-aerial volcanoes (e.g. Walker,
328 1993; Cashman et al., 1999), high eruption rates and low magma viscosities are the dominant causes
329 of long run-out lava flows. Extensive lava flows have also been observed at other deep-water
330 volcanoes and occur primarily because of the high hydrostatic pressure in deep-water environments



331 (e.g. Chadwick et al., 2018; Embley and Rubin, 2018; Ikegami et al., 2018). In particular, higher
332 ambient pressure can affect lava rheology (lower viscosity, vesicularity, crystal content), suppress
333 magma decompression and ascent, and, thereby, extrusion dynamics (Bridges, 1997; Gregg and
334 Fornari, 1998). For example, upon eruption of a 1200–1100°C basalt (MORB composition) at a
335 confining pressure of 20 MPa (i.e. a hydrostatic-equivalent water depth of 2 km), lava can contain
336 up to 1.4 wt% H₂O at equilibrium volatile solubility (Newman and Lowenstern, 2002). The resulting
337 lava viscosity of 9–38 Pa s is significantly lower than a dry (0.1 wt% H₂O) sub-aerial basalt, having
338 a viscosity range of 41–248 Pa s (calculated using Giordano et al., 2008). Higher H₂O content in
339 lavas erupted in deep-water, compared to those extruded in sub-aerial settings, will mean: (1) there
340 are fewer bubbles from suppressed degassing or brittle fragmentation to hinder flow (Gregg and
341 Fornari, 1998); (2) crystallization may be inhibited, reducing the effect of crystal interactions on
342 viscosity; and (3) the glass transition temperature is suppressed (Giordano et al. 2008), allowing
343 lavas to flow further.

344 From our seismic reflection data it is also clear channelization in lava tubes, in addition to the
345 water content effects described above, also facilitated long distance lava transport. We suggest these
346 tubes formed by rapid cooling and hardening of a surficial crust that insulated and focused lava flow
347 through a core channel (e.g. Cashman et al., 1999). Based on the long run-out lava distances, we
348 consider our initial assumption that the imaged volcanic features have a mafic composition remains
349 valid. Overall, whilst we do not know the composition of the lavas imaged in our seismic reflection
350 data, pressure-related changes in lava rheology and channelization of any lava type (i.e. mafic to
351 silicic) will allow it to flow hotter for longer. Given the downslope topographic controls during
352 eruption, a combination of rheology changes and channelization allowed lavas to flow for >9 km



353 from associated volcanic edifices.

354 The overall geometry and internal architecture of the imaged lava flows indicate substrate
355 rheology was a key control on emplacement dynamics. Our 3D seismic reflection data show that
356 relatively long run-out lava flows (>9 km) erupted from deep-water volcanoes have a rugged basal
357 surface that is locally defined by erosional basal 'ramps'. Truncation of underlying strata suggests
358 the lavas were able to erode down into the seabed, perhaps because the pre-eruption substrate was
359 cold, wet, and unconsolidated. We suggest erosion of the lava substrate was promoted by: (1) the
360 dense (bubble-poor) lava sinking down into or 'dredging' the soft sediments (Duffield et al., 1986;
361 Ikegami et al. 2018); (2) thermal erosion (Griffiths, 2000); and/or (3) more "turbulent" flow
362 dynamics of channelized lava, consistent with the inferred low viscosities (<10 Pa s).

363 Lava flows eventually ceased in distal areas due to gradual cooling and crystallization (Cashman
364 et al., 1999). We suggest that, in the case of the straight lava flows (C5 and C6), lava transported
365 within the axial tube temporarily accumulated at the transient end of the flow, possibly forming a
366 lava pool (Greeley, 1987). Lava entering the tube from the ongoing or new volcanic eruption caused
367 an increase in pressure, with the cooled and crystallized material at the flow toe forming an
368 impermeable, albeit, transient barrier. High hydrostatic pressure (>26 MPa at C5 and C6) and thick
369 surficial crusts inhibited the release of pressure build up by significant lava inflation (Gregg and
370 Fornari, 1998). Eventually, pressure build-up was sufficient to rupture this frontal, leading to
371 emplacement of a fan downdip of the front-most base-lava ramp (F5; Fig. 5a, 7-8) (Griffiths, 2000).
372 However, in the case of fans (e.g. F1-4) fed by sinuous channels (Figs. 4a-b), we suggest these were
373 emplaced in a process similar to that documented by Miles and Cartwright (2010), with lobate lava
374 flows fed and bisected by a 'lava tube' through magma inflation and increases in eruption rate. At



375 the end of sinuous lava flow channels (e.g. C1), the main channel bifurcated to form a lobate fan
376 (F3, Figs. 4a-b), which was also probably caused by flow branching triggered by magma cooling
377 (Griffiths, 2000).

378

379 **5.5. Volume balance of volcano edifice and lava flow**

380 Inaccurate constraints on total erupted volumes compromises our understanding of volcano
381 construction, lava propagation, eruption rates, eruption durations, magma storage conditions,
382 melting processes, and risk assessment of volcanism in deep-water settings (Carey et al., 2018).
383 High-resolution 3D seismic reflection data allow us to calculate the volumes of material contained
384 within volcano edifices and in flanking lava flows. We show that most (i.e. 50-97%) of the erupted
385 material is transported away from the imaged edifices, an observation comparable to that made for
386 deep-ocean volcanic eruptions (Caress et al., 2012; Carey et al., 2018). A critical outcome of our
387 work is that flanking lava flows, and to a lesser extent the volcanic edifices, have rugged and
388 discordant bases (Fig. 7); accurately calculating the volume of deep-water volcanoes and lava flows
389 therefore requires an understanding of their basal morphology. Erupted volume estimates based
390 solely on remote sensing of the seabed may be thus incorrect (e.g. Robinson and Eakins, 2006).
391 Although we show the accuracy of total erupted volume estimates can be improved by constraining
392 basal volcano and lava morphologies, seismic images capturing the geological record of deep-water
393 volcanoes cannot determine how much, if any, volcanic material was transported away from the
394 eruption site as pumice rafts (e.g. Carey et al. 2018). Nevertheless, 3D seismic imaging can
395 significantly improve quantitative volume estimates of recent and ancient volcanic features (e.g.
396 volcano edifices and lava flows) either currently on the seafloor or now buried by sedimentary



397 successions.

398

399 **6. Conclusions**

400 High-resolution 3-D seismic data from the South China Sea allow us to image and map the
401 internal structure, calculate the volume of erupted material, and to better understand the extrusion
402 dynamics of buried deep-water volcanoes; such insights cannot readily be gained from analysis of
403 remote sensing data. Volcanism occurred ~6.3–2.58 Ma, after seafloor spreading had ceased in the
404 area, and may be related to the Dongsha Event and/or a hypothesized Hainan mantle plume. High
405 hydrostatic pressure, an inclined seabed (~1°), and low-strength, very fine-grained, near-seabed
406 sediments, combined with formation of lava tubes and extrusion of low-viscosity magmas, are likely
407 responsible for observed long-distance lava run-outs (>9 km) in this deep-water environment. We
408 show the imaged volcanic edifices and associated lava flows have rugged, erosional bases, meaning
409 traditional remote sensing-based volume calculations of deep-water volcanic features, which
410 typically assume smooth bases, are underestimated. Because seismic reflection data images the base
411 of deep-water volcanoes and lava flows, we calculate a large amount (as high as ~97%) of the
412 erupted materials are transported away from the volcano edifices, suggesting that volume of deep-
413 water volcanic edifices may not faithfully archive eruption size or magma production. Considering
414 deep-water conditions (e.g. high hydrostatic pressure and unconsolidated sediments) in the study
415 area are common elsewhere, the conclusions derived from this study can likely be used in other
416 deep-water sedimentary basins and some mid-ocean ridges. Our study highlights that 3D seismic
417 reflection data can play a critical to understanding volcano morphology in 3D and accurately
418 estimating volume of erupted material.



419

420 **Author Contribution**

421 Qiliang Sun, Christopher A-L. Jackson, Craig Magee and Xinong Xie have contributed to the
422 conceptualization, data analysis, writing and revising the original draft. Samuel J. Mitchell have
423 contributed to the conceptualization and revising the original draft.

424

425 **Competing interests**

426 The authors declare that they have no conflict of interest.

427

428 **Acknowledgment**

429 This work was supported by the National Scientific Foundation of China (Grant Nos. 91528301,
430 41676051 and 41372112), the Programme of Introducing Talents of Discipline to Universities (No.
431 B14031) and the Fundamental Research Funds for the Central Universities-the China University of
432 Geosciences (Wuhan) (No. CUG160604). We thank the China National Offshore Oil Company
433 (CNOOC) for permission to release the data; reflection seismic data may be requested from CNOOC
434 (<http://www.cnooc.com.cn/en/>). Dieter Franke, Gerome Calvès and Nick Schofield are thanked for
435 their invaluable comments and suggestions. Rebecca Bell is thanked for generously providing office
436 space during the visit of Qiliang Sun to Imperial College.

437

438 **References**

439 Allen, R.W., Berry, C., Henstock, T.J., Collier, J.S., Dondin, F.J-Y., Rietbrock, A., Latchman, J.L., and Robertson,
440 R.E.A.: 30 Years in the Life of an Active Submarine Volcano: A Time - Lapse Bathymetry Study of the Kick-em-



- 441 Jenny Volcano, Lesser Antilles, *Geochem. Geophys. Geosy.*, 19, 715-731, <https://doi.org/10.1002/2017GC007270>,
- 442 2018.
- 443 Berndt, C., Skogly, O.P., Planke, S., Eldholm, O., and Mjelde, R.: High-velocity break up-related sills in the Vøring
- 444 Basin, off Norway, *J. Geophys. Res.*, 105, 28443-28454, <https://doi.org/10.1029/2000JB900217>, 2000.
- 445 Briais, A., Patriat, P., and Tapponnier, P.: Updated interpretation of magnetic anomalies and seafloor spreading stages
- 446 in the South China Sea: Implications for the Tertiary tectonics of Southeast Asia, *J. Geophys. Res.*, 98, 6299-6328,
- 447 <https://doi.org/10.1029/92JB02280>, 1993.
- 448 Bridges, N.T.: Ambient effects on basalt and rhyolite lavas under Venusian, subaerial, and subaqueous conditions, *J.*
- 449 *Geophys. Res.*, 102(E4), 9243-9255, <https://doi.org/10.1029/97JE00390>, 1997.
- 450 Brown, A.R.: Interpretation of three-dimensional seismic data: AAPG Memoir 42, 6th ed. SEG Investigations in
- 451 Geophysics, 2004.
- 452 Calvès, G., Schwab, A.M., Huuse, M., Clift, P.D., Gaina, C., Jolley, D., Tabrez, A.R., and Inam, A.: Seismic
- 453 volcanostratigraphy of the western Indian rifted margin: The pre-Deccan igneous province, *J. Geophys. Res.*, 116,
- 454 B01101, <https://doi.org/10.1029/2010JB000862>, 2011.
- 455 Calvès, G., Schwab, A.M., Huuse, M., van Rensbergen, P., Clift, P.D., Tabrez, A.R., and Inam, A.: Cenozoic mud
- 456 volcano activity along the Indus Fan: offshore Pakistan, *Basin Res.*, 22, 398-413, <https://doi.org/10.1111/j.1365->
- 457 2117.2009.00448.x, 2009.
- 458 Cameselle, A.L., Ranero, C.R., Franke, D., and Barckhausen, U.: The continent-ocean transition on the northwestern
- 459 South China Sea, *Basin Res.*, 29, 73-95, <https://doi.org/10.1111/bre.12137>, 2017.
- 460 Caress, D.W., Clague, D.A., Paduan, J.B., Martin, J.F., Dreyer, B.M., Chadwick Jr, W.W., Denny, A., and Kelley,
- 461 D.S.: Repeat bathymetric surveys at 1-metre resolution of lava flows erupted at Axial Seamount in April 2011,
- 462 *Nat. Geosci.*, 5, 483-488, <https://doi.org/10.1038/NGEO1496>, 2012.



- 463 Carey, R., Soule, S.A., Manga, M., White, J.D.L., McPhie, J., Wysoczanski, R., Jutzeler, M., Tani, K., Yoerger, D.,
464 Fornari, D., Caratori-Tontini, F., Houghton, B., Mitchell, S., Ikegami, F., Conway, C., Murch, A., Fauria, K., Jones,
465 M., Cahalan, R., and McKenzie, W.: The largest deep-ocean silicic volcanic eruption of the past century, *Sci. Adv.*,
466 4, e1701121, <https://doi.org/10.1126/sciadv.1701121>, 2018.
- 467 Cashman, K.V., Thornber, C.R., and Kauahikaua, J.P.: Cooling and crystallization of lava in open channels, and the
468 transition of pahoehoe lava to `a`a, *B. Volcanol.*, 61, 306-323, <https://doi.org/10.1007/s004450050>, 1999.
- 469 Chadwick Jr, W.W., Merle, S.G., Baker, E.T., Walker, S.L., Resing, J.A., Butterfield, D.A., Anderson, M.O.,
470 Baumberger, T. and Bobbitt, A.M.: A recent volcanic eruption discovered on the central Mariana back-arc
471 spreading center: *Front. Earth Sci.*, 6, 172, <https://doi.org/10.3389/feart.2018.00172>, 2018.
- 472 Chiu, M.: The p-wave velocity modeling of the transitional crust in northern South China Sea continental margin,
473 M.S. dissertation, National Taiwan Ocean University, Keelung, 112 pp., 2010.
- 474 Clift, P.D., Lin, J., and ODP Leg 184 Scientific Party: Patterns of extension and magmatism along the continent-
475 ocean boundary, South China margin, Geological Society, London, Special Publications, 187, 489-510,
476 <https://doi.org/10.1144/GSL.SP.2001.187.01.24>, 2001.
- 477 Cocchi, L., Masetti, G., Muccini, F., and Carmisciano, C.: Geophysical mapping of Vercelli Seamount: Implications
478 for Miocene evolution of the Tyrrhenian back arc basin, *Geosci. Front.*, 7, 835-849,
479 <https://doi.org/10.1016/j.gsf.2015.06.006>, 2016.
- 480 Ding, W.W., and Li, J.B.: Propagated rifting in the Southwest Sub-basin, South China Sea: Insights from analogue
481 modelling, *J. Geodyn.*, 100, 71-86, <https://doi.org/10.1016/j.jog.2016.02.004>, 2016
- 482 Duffield, W.A., Bacon, C.R., and Delaney, P.T.: Deformation of poorly consolidated sediment during shallow
483 emplacement of a basalt sill, Coso Range, California, *B. Volcanol.*, 48, 97-107,
484 <https://doi.org/10.1007/BF01046545>, 1986.



- 485 Embley, R.W. and Rubin, K.H.: Extensive young silicic volcanism produces large deep submarine lava flows in the
486 NE Lau Basin, *B. Volcanol.*, 80, 36, <https://doi.org/10.1007/s00445-018-1211-7>, 2018.
- 487 Expedition 349 Scientists: South China Sea tectonics: Opening of the South China Sea and its implications for
488 southeast Asian tectonics, climates, and deep mantle processes since the late Mesozoic, *International Ocean
489 Discovery Program Preliminary Report, 349*, <https://doi.org/10.14379/iodp.pr.349.2014>, 2014.
- 490 Fan, C.Y., Xia, S.H., Zhao, F., Sun, J.L., Cao, J.H., Xu, H.L., and Wan, K.Y.: New insights into the magmatism in
491 the northern margin of the South China Sea: Spatial features and volume of intraplate seamounts, *Geochem.
492 Geophys. Geosy.*, 18, 2216-2239, <https://doi.org/10.1002/2016GC006792>, 2017.
- 493 Francis, P.W. and Thorpe, R.S.: Significance of lithologic and morphologic variations of pyroclastic cones, *Geo. Soc.
494 Am. Bull.*, 85, 927-930, [https://doi.org/10.1130/0016-7606\(1974\)85<927:SOLAMV>2.0.CO;2](https://doi.org/10.1130/0016-7606(1974)85<927:SOLAMV>2.0.CO;2), 1974.
- 495 Franke, D.: Rifting, lithosphere breakup and volcanism: comparison of magma-poor and volcanic rifted margins,
496 *Marine and Petroleum Geology*, 43, 63-87, <https://doi.org/10.1016/j.marpetgeo.2012.11.003>, 2013.
- 497 Franke, D., Savva, D., Pubellier, M., Steuer, S., Mouly, B., Auxietre, J., Meresse, F., and Chamot-Rooke, N.: The
498 final rifting evolution in the South China Sea, *Mar. Petrol. Geol.*, v. 58, p. 704-720,
499 <https://doi.org/10.1016/j.marpetgeo.2013.11.020>, 2014.
- 500 Funck, T.: Structure of the volcanic apron north of Gran Canaria deduced from reflection seismic, bathymetric and
501 borehole data, Ph.D. dissertation, University of Kiel, 156 pp., 1996.
- 502 Giordano, D., Russell, J.K., Dingwell, D.B.: Viscosity of magmatic liquids: a model, *Earth Planet. Sci. Lett.*, 271,
503 123-134, <https://doi.org/10.1016/j.epsl.2008.03.038>, 2008.
- 504 Goto, Y., and McPhie, J.: Morphology and propagation styles of Miocene submarine basaltic lavas at Stanley,
505 northwestern Tasmania, Australia, *J. Volcanol. Geoth. Res.*, 130, 307-328, [https://doi.org/10.1016/S0377-0273\(03\)00311-1](https://doi.org/10.1016/S0377-0273(03)00311-1), 2004.



- 507 Grosse, P., and Kervyn, M.: Morphometry of terrestrial shield volcanoes, *Geomorphology*, 304, 1-14,
508 <https://doi.org/10.1016/j.geomorph.2017.12.017>, 2018.
- 509 Greeley, R.: The role of lava tubes in Hawaiian volcanoes, U.S. Geological Survey Professional Paper 1350, 1589-
510 1602, 1987.
- 511 Gregg, T.K.P., and Fornari, D.J.: Long submarine lava flows: Observations and results from numerical modeling, *J.*
512 *Geophys. Res.*, v. 103, p. 27517-27531, <https://doi.org/10.1029/98JB02465>, 1998.
- 513 Griffiths, R.W. and Fink, J.H.: Solidification and morphology of submarine lavas: A dependence on extrusion rate,
514 *J. Geophys. Res.*, 97(B13), 19729-19737, <https://doi.org/10.1029/92JB01594>, 1992.
- 515 Griffiths, R.W.: The Dynamics of lava flows, *Annu. Rev. Fluid Mech.*, 32, 477-518,
516 <https://doi.org/10.1146/annurev.fluid.32.1.477>, 2000.
- 517 Hall, R.: Cenozoic geological and plate tectonic evolution of SE Asia and the SW Pacific: Computer-based
518 reconstructions, model and animations, *J. Asian Earth Sci.*, 20, 353-431, [https://doi.org/10.1016/S1367-](https://doi.org/10.1016/S1367-9120(01)00069-4)
519 [9120\(01\)00069-4](https://doi.org/10.1016/S1367-9120(01)00069-4), 2002.
- 520 He, Y.M., and Wen, L.X.: Seismic velocity structures and detailed features of the D'' discontinuity near the core-
521 mantle boundary beneath eastern Eurasia, *Phys. Earth Planet. In.*, 189, 176-184,
522 <https://doi.org/10.1016/j.pepi.2011.09.002>, 2011.
- 523 Holcomb, R.T., Moore, J.G., Lipman, P.W., and Belderson, R.H.: Voluminous submarine lava flows from Hawaiian
524 volcanoes, *Geology*, 16, 400-404, [https://doi.org/10.1130/0091-7613\(1988\)016<0400:VSlava flow](https://doi.org/10.1130/0091-7613(1988)016<0400:VSlava flow fanH>2.3.CO;2)
525 [fanH>2.3.CO;2](https://doi.org/10.1130/0091-7613(1988)016<0400:VSlava flow fanH>2.3.CO;2), 1988.
- 526 Ikegami, F., McPhie, J., Carey, R., Mundana, R., Soule, S.A. and Jutzeler, M.: The eruption of submarine rhyolite
527 lavas and domes in the deep ocean—Havre 2012, Kermadec Arc, *Front. Earth Sci.*, 6, 147,
528 <https://doi.org/10.3389/feart.2018.00147>, 2018.



- 529 Jackson, C.A.-L.: Seismic reflection imaging and controls on the preservation of ancient sill-fed magmatic vents, *J.*
530 *Geol. Soc. London*, 169, 503-506, <https://doi.org/10.1144/0016-76492011-147>, 2012.
- 531 Judd, A.G., and Hovland, M. (Eds.): *Seabed Fluid Flow: The Impact on Geology, Biology and the Marine*
532 *Environment*, Cambridge University Press, Cambridge, 2007.
- 533 Lester, R., Van Avendonk, H.J.A., McIntosh, K., Lavier, L., Liu, C.S., Wang, T.K., and Wu, F.: Rifting and
534 magmatism in the northeastern South China Sea from wide-angle tomography and seismic reflection imaging: *J.*
535 *Geophys. Res.*, 119, 2305-2323, <https://doi.org/10.1002/2013JB010639>, 2014.
- 536 Li, C.F., Lin, J., Kulhanek, D.K., and the Expedition 349 Scientists: Proceedings of the International Ocean
537 Discovery Program, 349, <https://doi.org/10.14379/iodp.proc.349.103.2015>, 2015.
- 538 Li, C.F., Xu, X., Lin, J., Sun, Z., Zhu, J., Yao, Y.J., Zhao, X.X., Liu, Q.S., Kulhanek, D.K., Wang, J., Song, T.R.,
539 Zhao, J.F., Qiu, N., Guan, Y.X., Zhou, Z.Y., Williams, T., Bao, R., Briaies, A., Brown, E.A., Chen, Y.F., Clift, P.D.,
540 Colwell, F.S., Dadd, K.A., Ding, W.W., Almeida, I.H., Huang, X.L., Hyun, S., Jiang, T., Koppers, A.A.P., Li, Q.Y.,
541 Liu, C.L., Liu, Z.F., Nagai, R.H., Peleo-Alampay, A., Su, X., Tejada, M.L.G., Trin, H.S., Yeh, Y.C., Zhang, C.L.,
542 Zhang, F., and Zhang, G.L.: Ages and magnetic structures of the South China Sea constrained by the deep tow
543 magnetic surveys and IODP Expedition 349: *Geochem. Geophys. Geosy.*, 15, 4958-4983,
544 <https://doi.org/10.1002/2014JB011686>, 2014.
- 545 Li, L., Clift, P.D., and Nguyen, H.T.: The sedimentary, magmatic and tectonic evolution of the southwestern South
546 China Sea revealed by seismic stratigraphic analysis, *Mar. Geophys. Res.*, 34, 341-365,
547 <https://doi.org/10.1007/s11001-013-9171-y>, 2013.
- 548 Li, P., and Liang, H.: Cenozoic magmatism in the Pearl River Mouth Basin and its relationship to the basin evolution
549 and petroleum accumulation, *Guangdong Geology*, 9, 23-34, 1994.
- 550 Lüdmann, T., and Wong, H.K.: Neotectonic regime on the passive continental margin of the northern South China



- 551 Sea, *Tectonophysics*, 311, 113-138, [https://doi.org/10.1016/S0040-1951\(99\)00155-9](https://doi.org/10.1016/S0040-1951(99)00155-9), 1999.
- 552 Lüdmann, T., Wong, H.K., and Wang, P.: Plio-Quaternary sedimentation processes and neotectonics of the northern
553 continental margin of the South China Sea, *Mar. Geol.*, 172, 331-356, <https://doi.org/10.1016/S0025->
554 [3227\(00\)00129-8](https://doi.org/10.1016/S0025-3227(00)00129-8), 2001.
- 555 Magee, C., Hunt-Stewart, E., and Jackson, C.A.-L.: Volcano growth mechanisms and the role of sub-volcanic
556 intrusions: Insights from 2D seismic reflection data, *Earth Planet. Sci. Lett.*, 373, 41-53,
557 <https://doi.org/10.1016/j.epsl.2013.04.041>, 2013.
- 558 Miles, A., and Cartwright, J.: Hybrid flow sills: A new mode of igneous sheet intrusion, *Geology*, 38, 343-346,
559 <https://doi.org/10.1130/G30414.1>, 2010.
- 560 Newman, S., and Lowenstern, J.B.: VolatileCalc: a silicate melt-H₂O-CO₂ solution model written in Visual Basic for
561 excel, *Comput. Geosci.*, 28, 597-604, [https://doi.org/10.1016/S0098-3004\(01\)00081-4](https://doi.org/10.1016/S0098-3004(01)00081-4), 2002,
- 562 Planke, S., Symonds, P., Alvestad, E., and Skogseid, J.: Seismic volcanostratigraphy of large-volume basaltic
563 extrusive complexes on rifted margins, *J. Geophys. Res.*, 105, 19335-19351,
564 <https://doi.org/10.1029/1999JB900005>, 2000.
- 565 Qin, G.Q.: Application of micropaleontology to the sequence stratigraphic studies of late Cenozoic in the Pearl River
566 Mouth Basin, *Marine Geology & Quaternary Geology*, 16, 1-18, <https://doi.org/10.16562/j.cnki.0256->
567 [1492.199.04.001](https://doi.org/10.16562/j.cnki.0256-1492.199.04.001), 1996.
- 568 Reynolds, P., Holford, S., Schofield, N., and Ross, A.: Three-dimensional seismic imaging of ancient submarine lava
569 flows: an example from the southern Australian margin, *Geochem. Geophys. Geosy.*, 18, 3840-3853,
570 <https://doi.org/10.1002/2017GC007178>, 2017.
- 571 Reynolds, P., Schofield, N., Brown, R.J. and Holford, S.P.: The architecture of submarine monogenetic volcano-
572 insights from 3D seismic data, *Bas. Res.*, 30, 437-451, <https://doi.org/10.1111/bre.12230>, 2018.



- 573 Robinson, J.E., and Eakins, B.W.: Calculated volumes of individual shield volcanoes at the young end of the
574 Hawaiian Ridge, *J. Volcanol. Geoth. Res.*, 151, 309-617, <https://doi.org/10.1016/j.jvolgeores.2005.07.033>, 2006.
- 575 Ru, K., and Pigott, J.D.: Episodic rifting and subsidence in the South China Sea, *AAPG Bull.*, 9, 1136-1155, 1986.
- 576 Shi, X., Kohn, B., Spencer, S., Guo, X., Li, Y., Yang, X., Shi, H., Gleadow, A.: Cenozoic denudation history of
577 southern Hainan Island, South China Sea: constraints from low temperature thermochronology, *Tectonophysics*,
578 504, 100-115, <https://doi.org/10.1016/j.tecto.2011.03.007>, 2011.
- 579 Sibuet, J.-C., Yeh, Y.-C., and Lee, C.-S.: Geodynamics of the South China Sea, *Tectonophysics*, 692, 98-119,
580 <https://doi.org/10.1016/j.tecto.2016.02.022>, 2016.
- 581 Somoza, L., Gonzalez, F.J., Barker, S.J., Madureira, P., Medialdea, T., de Ignacio, C., Lourenco, N., Leon, R.,
582 Vazquez, J.T., and Palomino, D.: Evolution of submarine eruptive activity during the 2011-2012 El Hierro event
583 as documented by hydroacoustic images and remotely operated vehicle observations, *Geochem. Geophys. Geosy.*,
584 18, 3109-3137, <https://doi.org/10.1002/2016GC006733>, 2017.
- 585 Sun, Q.L., Xie, X.N., Piper, D.J.W., Wu, J., and Wu, S.G.: Three dimensional seismic anatomy of multi-stage mass
586 transport deposits in the Pearl River Mouth Basin, northern South China Sea: Their ages and kinematics, *Mar.*
587 *Geol.*, 393, 93-108, <https://doi.org/10.1016/j.margeo.2017.05.005>, 2017.
- 588 Sun, Q.L., Wu, S.G., Cartwright, J., Wang, S.H., Lu, Y.T., Chen, D.X., and Dong, D.D.: Neogene igneous intrusions
589 in the northern South China Sea: evidence from high resolution three dimensional seismic data, *Mar. Petrol. Geol.*,
590 54, 83-95, <https://doi.org/10.1016/j.marpetgeo.2014.02.014>, 2014b.
- 591 Sun, Q.L., Wu, S.G., Cartwright, J., and Dong, D.D.: Shallow gas and focused fluid flow systems in the Pearl River
592 Mouth Basin, northern South China Sea, *Mar. Geol.*, 315-318, 1-14, <https://doi.org/10.1016/j.margeo.2012.05.003>,
593 2012.
- 594 Sun, Z., Xu, Z., Sun, L., Pang, X., Yan, C., Li, Y., Zhao, Z., Wang, Z., Zhang, C.: The mechanism of post-rift fault



- 595 activities in the Baiyun Sag, Pearl River Mouth Basin, *J. Asian Earth Sci.*, 89, 76-87,
596 <https://doi.org/10.1016/j.jseas.2014.02.018>, 2014a.
- 597 Taylor, B., and Hayes, D.E.: Origin and history of the South China Sea Basin, in: *The Tectonic and Geologic*
598 *Evolution of Southeast Asian Seas and Islands*, edited by Hayes, D.E.. AGU, Washington, DC, 23-56, 1983.
- 599 Thomson, K.: Determining magma flow in sills, dykes and laccoliths and their implications for sill emplacement
600 mechanisms, *B. Volcanol.*, 70, 183-201, <https://doi.org/10.1007/s00445-007-0131-8>, 2007.
- 601 Thomson, K., and Hutton, D.: Geometry and growth of sill complexes: Insights using 3-D seismic from the North
602 Rockall Trough, *B. Volcanol.*, 66, 364–375, <https://doi.org/10.1007/s00445-003-0320-z>, 2004.
- 603 Tu, K., Flower, M.F.J., Carlson, R.W., Zhang, M., Xie, G.: Sr, Nd, and Pb isotopic compositions of Hainan basalts
604 (south China): implications for a subcontinental lithosphere Dupal source, *Geology*, 19, 567-569,
605 [https://doi.org/10.1130/0091-7613\(1991\)019<0567:SNAPIC>2.3.CO;2](https://doi.org/10.1130/0091-7613(1991)019<0567:SNAPIC>2.3.CO;2), 1991.
- 606 Wang, T.K., Chen, M.K., Lee, C.S., and Xia, K.Y.: Seismic imaging of the transitional crust across the northeastern
607 margin of the South China Sea, *Tectonophysics*, 412, 237-254, <https://doi.org/10.1016/j.tecto.2005.10.039>, 2006.
- 608 Wang, P., Prell, W.L., and ODP 184 scientists.: *Proceedings of the Ocean Drilling Program, Initial Reports*, 184.
609 Ocean Drilling Program, College Station, TX 2000, 2000.
- 610 Walker, G.P.L.: Basaltic-volcano systems, in: *Magmatic Processes and Plate Tectonics*, edited by Pritchard, H.M.,
611 Alabaster, T., Harris, N.B.W., and Neary, C.R., Geological Society Special Publication, 76, 3-38, 1993.
- 612 Wei, X.D., Ruan, A.G., Zhao, M.H., Qiu, X.L., Li, J.B., Zhu, J.J., Wu, Z.L., and Ding, W.W.: A wide-angle OBS
613 profile across the Dongsha uplift and Chaoshan depression in the mid-northern South China Sea, *Chinese J.*
614 *Geophys-CH.*, 54, 3325-3335, <https://doi.org/10.3969/j.issn.0001-5733.2011.12.030>, 2011.
- 615 Wu, S.G., Gao, J.W., Zhao, S.J., Lüdmann, T., Chen, D.X., and Spence, G.: Post-rift uplift and focused fluid flow in
616 the passive margin of Northern South China Sea, *Tectonophysics*, 615-616, 27-39,



- 617 <https://doi.org/10.1016/j.tecto.2013.12.013>, 2014.
- 618 Xia, S.H., Zhao, D.P., Sun, J.L., and Huang, H.B.: Teleseismic imaging of the mantle beneath southernmost China:
619 new insights into the Hainan plume, *Gondwana Res.*, 36, 33-43, <https://doi.org/10.1016/j.gr.2016.05.003>, 2016.
- 620 Xie, Z.Y., Sun, L.T., Pang, X., Zheng, J.Y., and Sun, Z.: Origin of the Dongsha Event in the South China Sea: Mar.
621 *Geophys. Res.*, 38, 357-371, <https://doi.org/10.1007/s11001-017-9321-8>, 2017.
- 622 Xu, S.C., Yang, S.K., and Huang, L.F.: The application of sequence stratigraphy to stratigraphic correlation, *Earth*
623 *Sci. Front.*, 2, 115-123, 1995.
- 624 Yan, P., Deng, H., Liu, H.L., Zhang, Z., and Jiang, Y.: The temporal and spatial distribution of volcanism in the South
625 China Sea region, *J. Asian Earth Sci.*, 27, 647-659, <https://doi.org/10.1016/j.jseaes.2005.06.005>, 2006.
- 626 Yan, P., Wang, Y.L., Liu, J., Zhong, G.J., and Liu, X.J.: Discovery of the southwest Dongsha Island mud volcanoes
627 amid the northern margin of the South China Sea, *Mar. Petrol. Geol.*, 88, 858-870,
628 <https://doi.org/10.1016/j.marpetgeo.2017.09.021>, 2017.
- 629 Yan, P., Zhou, D., and Liu, Z.S.: A crustal structure profile across the northern continental margin of the South China
630 Sea, *Tectonophysics*, 338, 1-21, [https://doi.org/10.1016/S0040-1951\(01\)00062-2](https://doi.org/10.1016/S0040-1951(01)00062-2), 2001.
- 631 Yang, S., Qiu, Y., and Zhu, B.: Atlas of Geology and Geophysics of the South China Sea, China Navigation
632 Publications, Tianjin, 2015.
- 633 Yu, H.S.: Structure, stratigraphy and basin subsidence of Tertiary basins along the Chinese southeastern continental
634 margin, *Tectonophysics*, 253, 63-76, 1994.
- 635 Zhang, N., and Li, Z.X.: Formation of mantle “lone plumes” in the global downwelling zone - A multiscale modelling
636 of subduction-controlled plume generation beneath the South China Sea, *Tectonophysics*, 723, 1-13,
637 <https://doi.org/10.1016/j.tecto.2017.11.038>, 2018.
- 638 Zhao, F., Alves, T.M., Wu, S.G., Li, W., Huuse, M., Mi, L.J., Sun, Q.L., and Ma, B.J.: Prolonged post-rift magmatism



639 on highly extended crust of divergent continental margins (Baiyun Sag, South China Sea), *Earth Planet. Sci. Lett.*,

640 445, 79-91, <https://doi.org/10.1016/j.epsl.2016.04.001>, 2016.

641 Zhao, F., Wu, S.G., Sun, Q.L., Huuse, M., Li, W., and Wang, Z.J.: Submarine volcanic mounds in the Pearl River

642 Mouth Basin, northern South China Sea, *Mar. Geol.*, 355, 162-172, <https://doi.org/10.1016/j.margeo.2014.05.018>,

643 2014.

644 Zhao, S.J., Wu, S.G., Shi, H.S., Dong, D.D., Chen, D.X., and Wang, Y.: Structures and dynamic mechanism related

645 to the Dongsha Event at the northern margin of the South China Sea, *Progress in Geophysics*, 27, 1008-1019,

646 <https://doi.org/10.6038/j.issn.1004-2903.2012.03.022>, 2012.

647 Zou, H., Li, P., and Rao, C.: Geochemistry of Cenozoic volcanic rocks in Zhu Jiangkou Basin and its geodynamic

648 significance, *Geochimica*, 24, 33-45, 1995.

649

650

651 **Tables**

652

653 Table 1: Dimensions of volcano edifices. ^adiameter and dip are average values.

Volcano edifice	^a Diameter/m	Height/m	Area/km ²	Volume/km ³	^a Dip/°
Volcano edifice 1 (V1)	3018	404±101	7.15	0.940±0.235	15.0±3.6
Volcano edifice 1 (V2)	714	200±50	0.44	0.030±0.008	27.8±5.9

654

655 Table 2: Dimensions of lava flow apron. ^aDiameter is calculated from the area as a circle. V =

656 Volcano edifice.

Lava flow apron	Diameter (m)	Area (km ²)	Thickness (m)	Volume (km ³)	Feeder	Shape
Lava flow apron	3182 ^a	7.95	80±20	0.637±0.159	V1	Ring

657

658 Table 3: Dimensions of lava flow channels (C). Please note that all the lengths of lava flow

659 channels are measured along their axes. ^aMaximum lengths (including the inferred part of lava660 flow channels); ^bMinimum length (C3 extends beyond the 3D survey); ^cThickneses cannot be

661 measured, because of lava flow channels (C1 and C2) are only identified on the plan-view map

662 (RMS and variance slice map); ^dArea and volume don't include the inferred part of C5.

Lava flow channels		Length (km)	Width (m)	Thickness (m)	Area (km ²)	Volume (km ³)
Volcano edifices 1-related	C1	2.86 ^a	55-273	unknown ^c	0.31 ^a	unknown ^c
	C2	3.66 ^a	94-340	unknown ^c	0.56 ^a	unknown ^c
	C3	4.60 ^b	163-340	52±13	0.84 ^a	0.044±0.011
Volcano edifices 2-related	C4	2.80	172-229	61±15	0.54	0.032±0.008
	C5	9.15 ^a	185-267	64±16	1.52 ^d	0.097±0.024 ^d
	C6	6.39	203-285	60±15	1.47	0.088±0.022
	C7	1.93	236-427	57±14	0.67	0.037±0.009

663

664 Table 4: Dimensions of lava flow fans. ^aDiameter is calculated from the area as a circle.



665 ^bMinimum areas and volumes, because of limited data coverage. C = Lava flow channel; S = Sill.

Lava flow fans	Diameter (m)	Area (km ²)	Thickness (m)	Volume (km ³)	Feeder	Shape
Lava flow fan 1 (F1)	944 ^a	0.70	41±10	0.028±0.007	C1	Lobate
Lava flow fan 2 (F2)	1050 ^a	0.87	41±10	0.035±0.009	C1	Lobate
Lava flow fan 3 (F3)	997 ^a	0.78 ^b	41±10	0.031±0.008 ^b	C1	Lobate
Lava flow fan 4 (F4)	2171 ^a	3.70 ^b	41±10	0.148±0.037 ^b	C2	Lobate
Lava flow fan 5 (F5)	3054 ^a	7.32	109±27	0.791±0.198	C5/C6	Lobate
Lava flow fan 6 (F6)	7906 ^a	49.07 ^b	55±14	2.650±0.662 ^b	S1/S2	Lobate

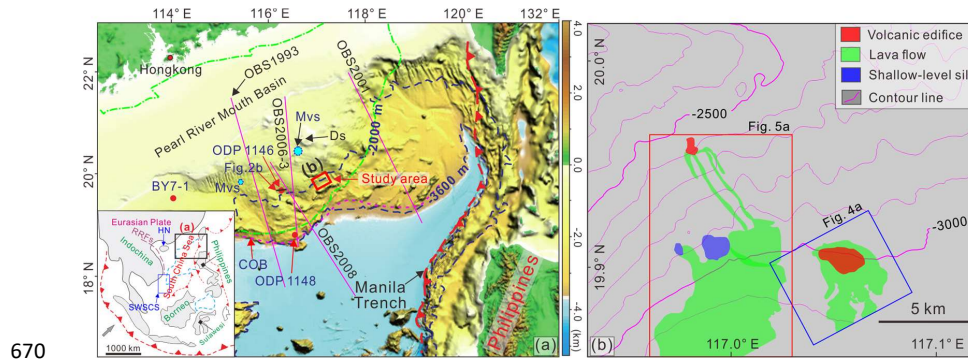
666

667



668 **Figures**

669



670

671 Figure 1: Geological setting of the study area. (a) Bottom left: regional setting of the South China

672 Sea that is bounded by the Red River Strike-slip faults (RRFs) to the west and by the subduction

673 trench (Manila Trench) to the east. Hainan Island (HN; Tu et al., 1991; Shi et al., 2011) and

674 southwestern South China Sea (SWSCS; Li et al., 2013) in which the magmatism has the similar

675 ages with the studied volcanoes are labelled. The study area (marked with red square) is located to

676 the south of Dongsha Islands. The green dashed line outlines the boundary of Pearl River Mouth

677 Basin. Locations of boreholes (Exploration well BY7-1 and ODP sites 1146 and 1148), crustal

678 structure profiles (OBS1993 (Yan et al., 2001), OBS2001 (Wang et al., 2006), OBS2006-3 (Wei et

679 al., 2011), and OBS2008 (Chiu, 2010)) and mud volcanoes (Mvs; Sun et al., 2012; Yan et al., 2017)

680 are labeled. Ds = Dongsha Islands; COB = Continent ocean boundary (Adopted from Sibuet et al.,

681 2016).The base map is modified from Yang et al. (2015); (b) Seabed morphologies of the study area.

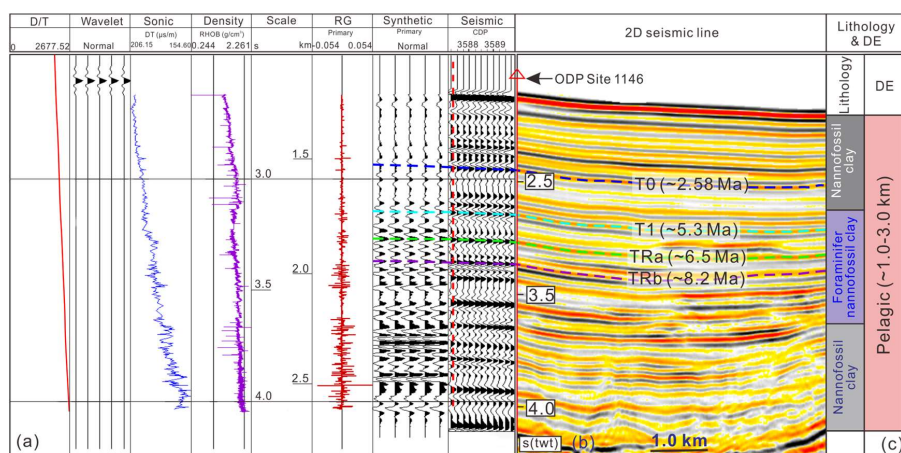
682 Distributions of volcano edifices (red), sills (blue), lava flows (green) and locations of Figures 4a

683 and 5a are labeled. The contour lines are in 100 ms (tw).t

684



685

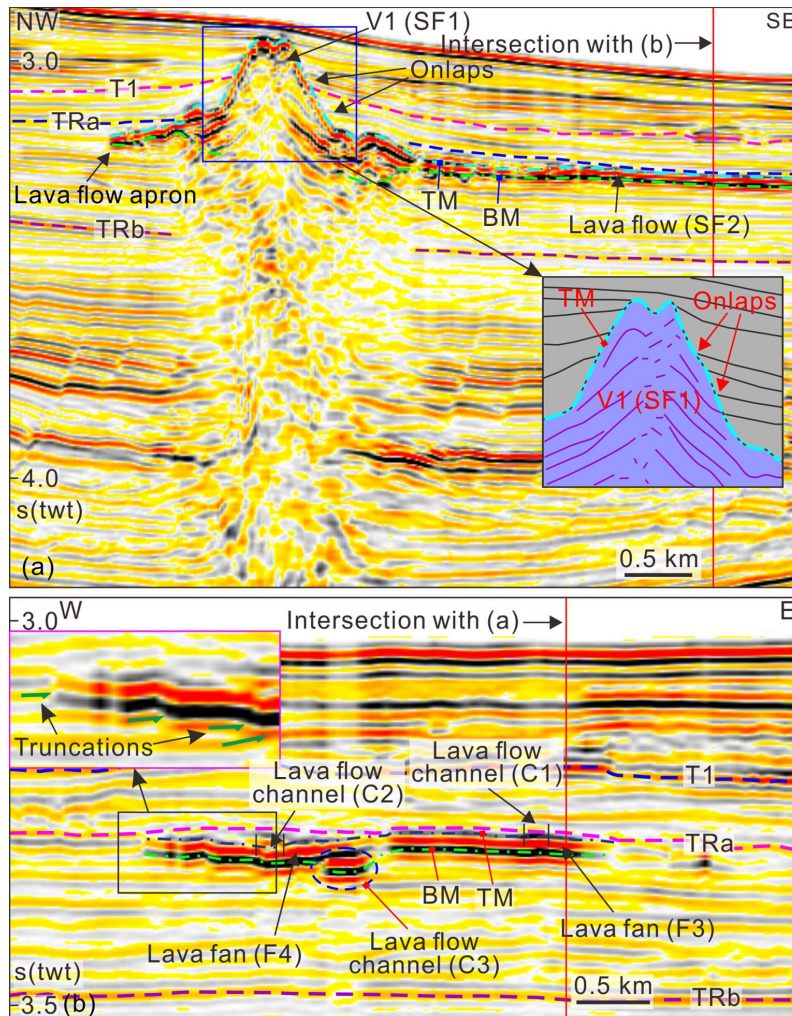


686

687 Figure 2: (a) Synthetic seismogram of ODP Site 1146 (Modified from Sun et al., 2017); (b) Seismic
 688 profile crossing through ODP Site 1146. The four seismic surfaces (T0 (~2.58 Ma), T1 (~5.3 Ma),
 689 TRa (~6.5 Ma) and TRb (~8.2 Ma)) are labeled. D/T =Depth/time; DT =interval transit time; RHOB
 690 = lithologic density; RC = reflection coefficient; (c) Lithology and depositional environment (DE)
 691 of ODP Site 1146 (Modified from Wang et al. (2000) and Clift et al. (2001)).
 692



693



694

695 Figure 3: Seismic characteristics of deep-water volcano (V1) and associated lava flow channels/fans.

696 (a) Seismic profile crosscuts the volcano edifice and associated lava flow; (b) Seismic profile

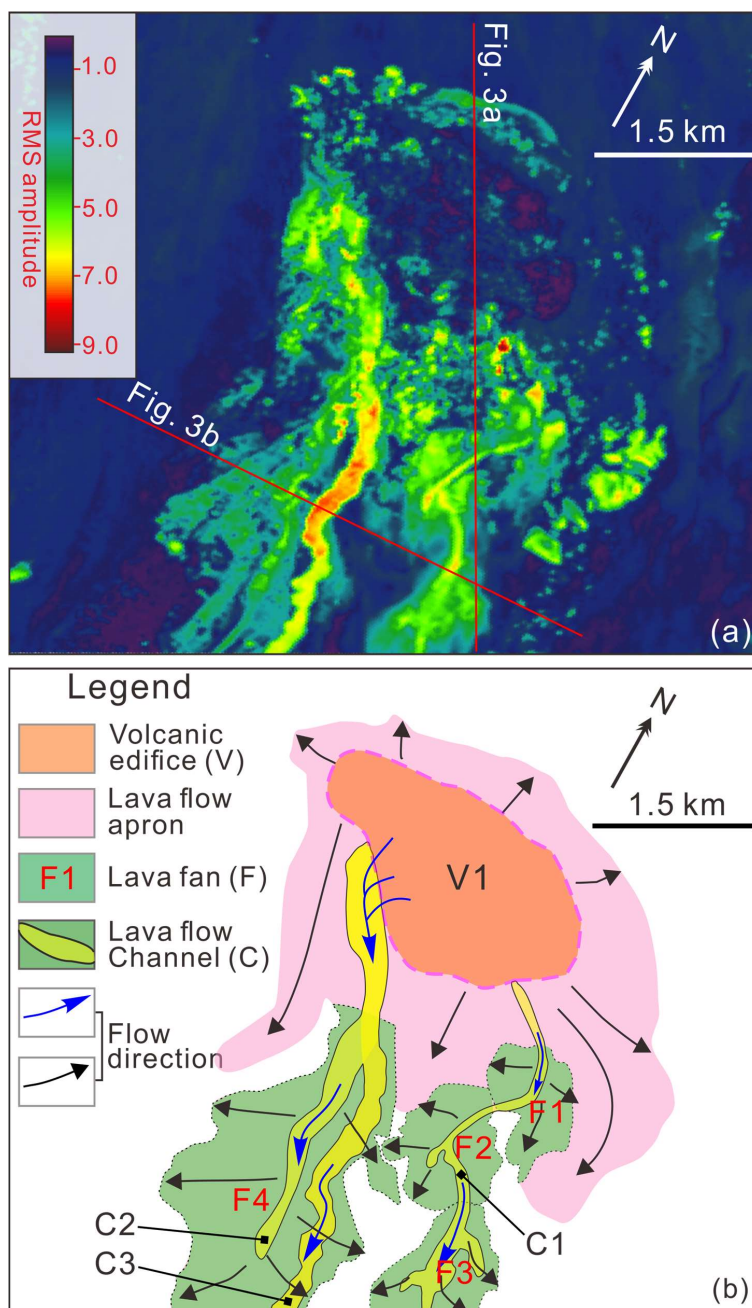
697 crosscuts the lava flow (enhanced seismic anomalies). TM = top of volcano/lava flow; BM = base

698 of volcano/lava flow. See locations in Figure 4.

699



700



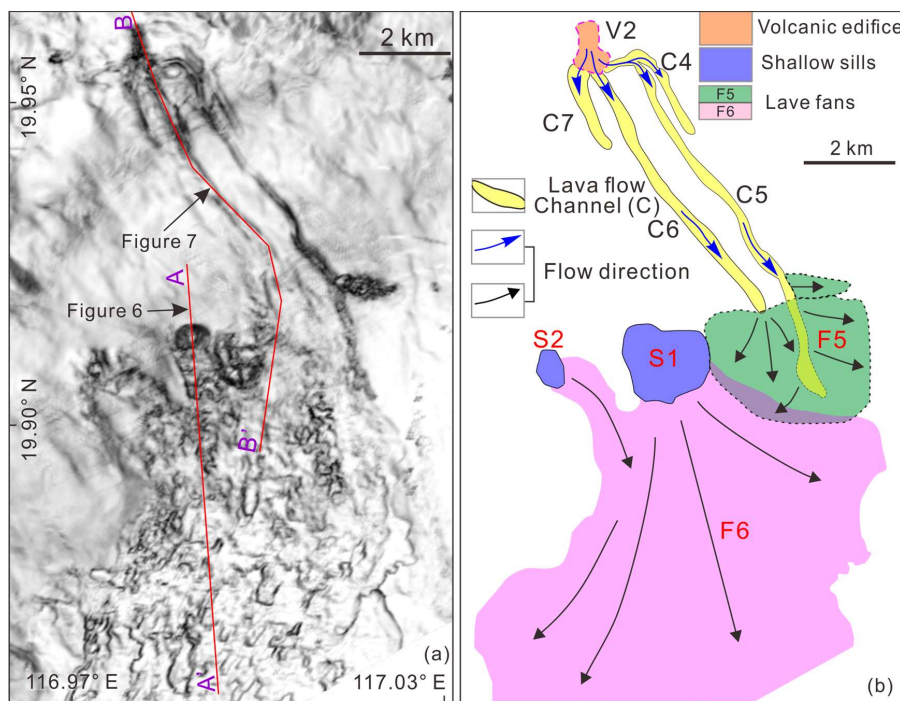
701

702 Figure 4: (a) and (b) RMS amplitude map (± 30 ms along the surface BM) and its interpretations.

703 Volcanic apron, lava flow channels/fans are labeled. See location in Figure 1b.



704



705

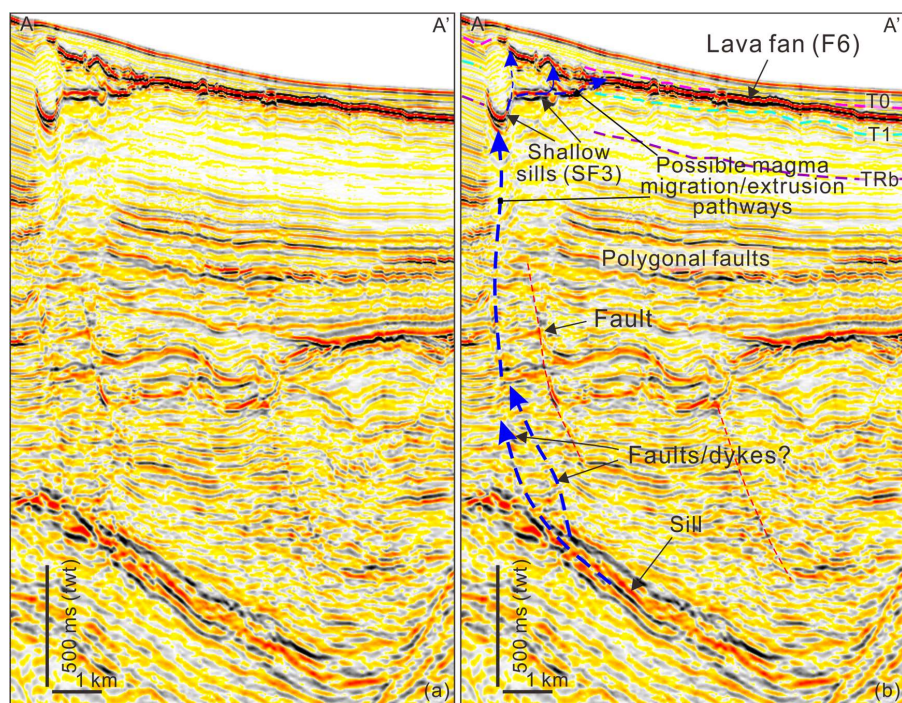
706 Figure 5: (a) and (b) Variance slice (extracted from the surface BM) and its interpretations. Lava

707 flows are clearly identified and marked. C = lava flow channel; S = shallow sill; F = lava fan.

708



709



710

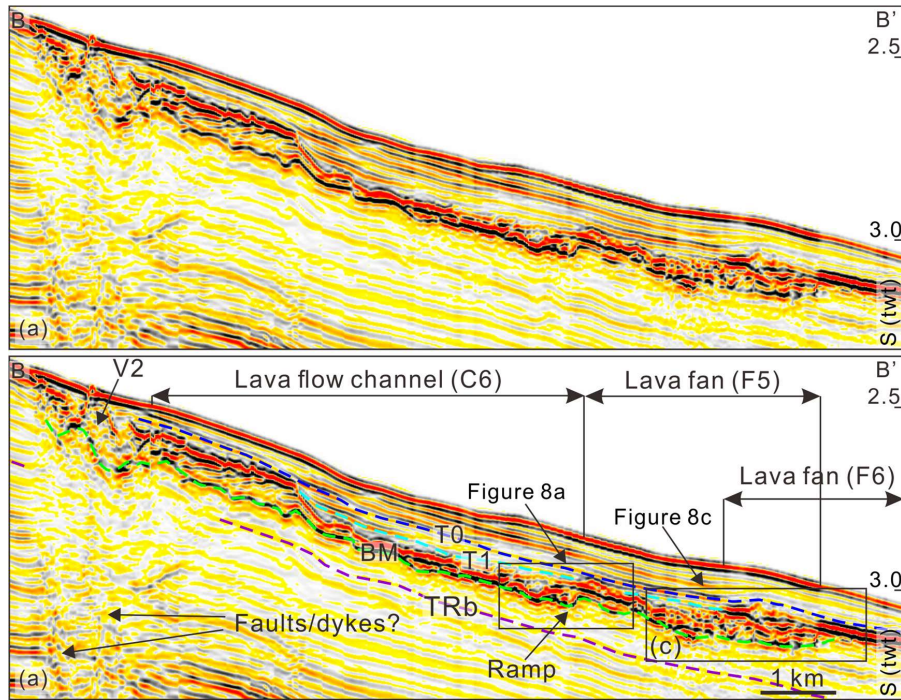
711 Figure 6: Seismic profile (a) and its interpretation show magma plumbing system from deep-seated

712 sill, shallow sill (S1) and lava fan (F6). See location in Figure 5a.

713



714



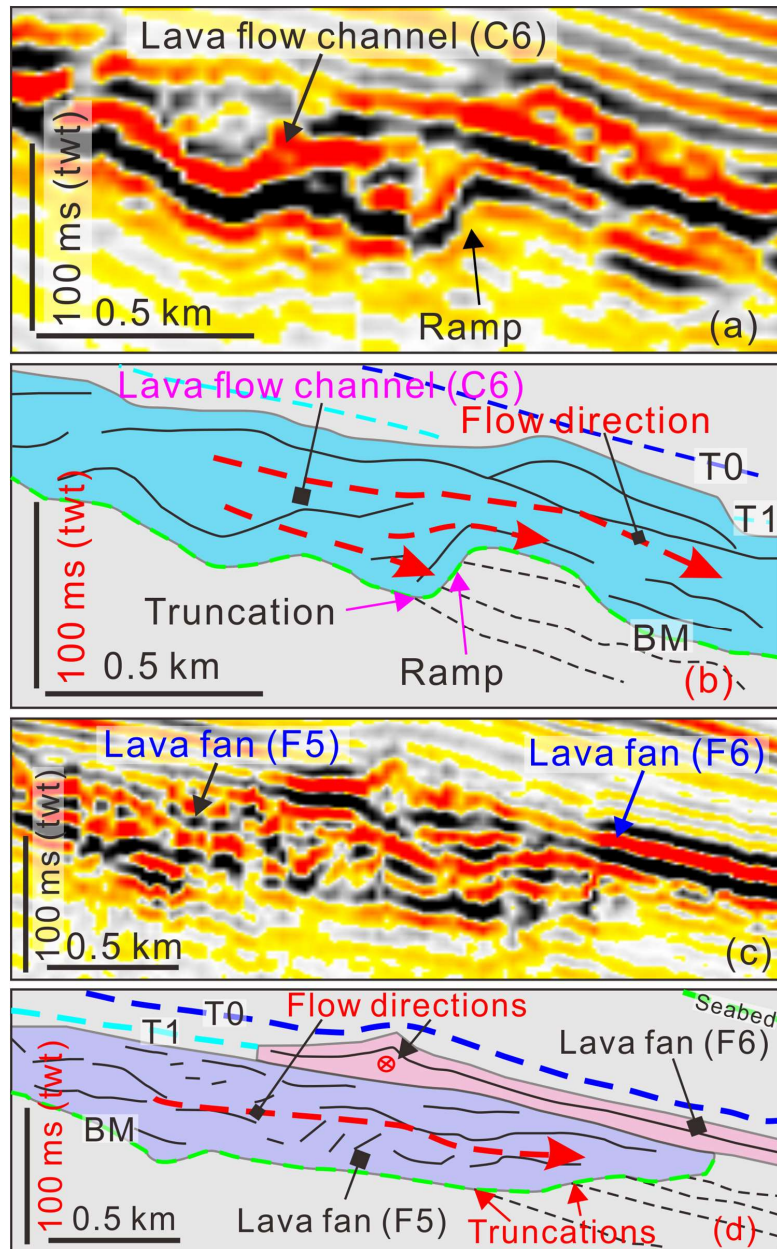
715

716 Figure 7: (a) Seismic profile crosscuts V2 and along lava flow channel (C6) and Lava fans (F5 and

717 F6). The V2 has a sharp boundary to the upslope. Lava fan 6 (F6) is directly overlying the Lava fan

718 5 (F5). BM = base of volcano/lava flow; See location in Figure 5a.

719



720

721 Figure 8: (a) and (b) Enlargement of the end of lava flow channel (ramp structure) and its line

722 drawings; (c) and (d) Enlargement and its line drawings of the lava fans (F5 and F6). BM = base of

723 volcano/lava flow. See locations in Figure 7.